Saeedian, Meysam; Taheri, Shamsodin; Pouresmaeil, Edris

Double–Stage photovoltaic generator augmented with FLL–based synthetic inertia emulator

Published in:
Electric Power Systems Research

DOI:
10.1016/j.epsr.2021.107715

Published: 01/03/2022

Document Version
Publisher's PDF, also known as Version of record

Electric Power Systems Research 204 (2022) 107715

Contents lists available at ScienceDirect

Electric Power Systems Research

journal homepage: www.elsevier.com/locate/epsr

Double–Stage photovoltaic generator augmented with FLL–based synthetic inertia emulator

Meysam Saeedian [a], Shamsodin Taheri [b], Edris Pouresmaeil [*,a]

[a] Department of Electrical Engineering and Automation, Aalto University, Espoo, Finland
[b] Department of Computer Science and Engineering, Universite' du Qu'ebec en Outaouais, Gatineau, Canada

ARTICLE INFO

Keywords:
Renewable energy source (RES) integration
Grid interfaced inverter
Virtual inertia
Frequency stability

ABSTRACT

Distributed virtual inertia (DVI) is a promising method in frequency support provision for power system transition toward ≈ 100% power electronic–based generation. In this approach, the inertia power is provided by discharging or charging dc capacitors adhered to the grid–tied inverters distributed in the grid. However, the dc–bus voltage drifts with the time from its nominal in the conventional DVI technique. Herein, we suggest a modified DVI–based frequency regulator which addresses the aforesaid issue. The inverter controller comprises two main loops: 1) inner current loop and 2) outer voltage loop augmented with the proposed synthetic inertia emulator, whereby measured grid frequency oscillations are transmuted to the synthetic inertia support. The proposed controller is utilized in a double–stage photovoltaic generator. The synchronization of generator with the host grid is performed using a fast but accurate frequency–locked loop (FLL) implemented in the synchronous reference frame. The small–signal state–space realization illustrates that the generator stability is scarcely sensitive to the dc–link capacitance changes, while the grid strength and the FLL controller gains significantly affect the stability. The efficacy of the proposed control scheme is verified by time–domain simulation results in MATLAB/Simulink. The grid frequency response depicts that the frequency rate of change is improved by 14.6% if the proposed synthetic inertia emulator is employed.

1. Introduction

1.1. Motivation

The ongoing power generation from RESs imposes new challenges on power system operation and control. Paramount among them, are inertia and governor droop requirements as SG–based power plants are replacing with converter–interfaced generators, resulting in detrimental impacts on the transient response in power systems following critical disturbances [1,2]. Thus, faster dynamics and larger frequency oscillations occur. To mitigate potential stability issues and increase the resilience of low–inertia grids, new ancillary services are required (e.g., synthetic or virtual inertia emulator) [3]. The provision of synthetic inertia is possible by VSCs operating in *grid–forming* or *grid–following* modes with a general mechanism as follow; the controller manipulates the converter power injection in response to the frequency disturbance so as limits the frequency nadir and the RoCoF level [4]. The increase (decrease) in power is supplied (stored) by the dc–side energy buffer.

1.2. Literature review

A plethora of devices have hitherto been proposed for generation–-side inertia emulation, categorizing as: 1) synchronous condensers (SCs), 2) virtual synchronous machines (VSMs), 3) wind turbines, 4) energy storage systems (batteries, ultra–capacitors (UCs), superconducting magnetic energy storage, etc.), and 5) converters dc–link capacitors. Utilizing backup SGs with partial loading - i.e., spinning reserve - or SCs is a direct method for system inertia augmentation. The study in [5] introduces the control of frequency swing dynamics through voltage channel. Therein, a two–band power system stabilizer adaptively adjusts reference voltage of a SC aimed at damping low–frequency oscillations and primary response control. Nevertheless, SCs yield high capital and operating cost. Ref. [6] describes the *grid–forming* VSM, so–called synchronverter - a method that maps SGs dynamics onto converter controller; i.e., the dynamic equations of an SG and a synchronverter are the same. Only the mechanical power exchanged with the prime mover is replaced with the power exchanged with the converter dc bus. Compared to an SG, we can choose the parameters such as inertia in the synchronverter. Pertinent to this device, [7] adds a

* Corresponding author.
E-mail address: edris.pouresmaeil@aalto.fi (E. Pouresmaeil).

https://doi.org/10.1016/j.epsr.2021.107715
Received 6 July 2021; Received in revised form 11 October 2021; Accepted 6 December 2021
Available online 15 December 2021

Nomenclature

Abbreviations

MPPT	Maximum power point tracking
PoI	Point of interconnection
RoCoF	Rate of change of frequency
SG	Synchronous generator
SRF	Synchronously–rotating reference frame
VSC	Voltage source converter

Variables

$\boldsymbol{i}$	Grid current space vector
$\boldsymbol{i_w}$	Converter current space vector
i_{pv}, i_{dc}	PV current, inverter dc–side current
$p_w(q_w), p_{pv}$	Converter output power, PV power
$\boldsymbol{u_g}$	Grid voltage space vector
$\boldsymbol{u_p}$	PoI voltage space vector
$\boldsymbol{u_w}$	Converter voltage space vector
u_{pv}, u_{dc}	PV voltage, dc–link voltage
ω	Grid angular frequency
δ	Synchronization angle

Parameters

C_{dc}, C_f	dc–link capacitance, filter capacitance
k_f	Frequency regulator gain
k_{fll}, d_{fll}	FLL controller gains
k_{pi}, k_{ii}	Current controller gains
k_{pu}, k_{iu}	Voltage controller gains
k_{puf}, k_{iuf}	Voltage recovery gains
$\boldsymbol{i_w}^\star$	VSC current reference space vector
$p_w^\star, q_w^\star$	Converter output power references
R_f, R_g	Filter resistance, grid resistance
L_f, L_g	Filter inductance, grid inductance
$u_{dc}^\star$	dc–link voltage reference
ω_0	Grid nominal angular frequency

damping correction loop to the synchronverter. It also proposes a method to compute the controller parameters, resulting in desired transient and steady–state responses. Analogous to the synchronverter and motivated by working principles of inductions machines, inducverter is introduced in [8]. The participation in the frequency regulation is fulfilled by a PLL–less swing equation–based approach in the inducverter; and the grid angle information is obtained via power damping unit. Akin to SGs, variable–speed wind turbine generators (VSWTGs) enjoy large amount of kinetic energy retained in their blades. However, a VSWTG does not naturally participate in frequency control due to the converter interface. Hence, supplementary loops are needed to be added to the power conversion system of such units [9]. Ref. [10] adjusts the turbine torque set point in line with the RoCoF level and frequency oscillations, allowing VSWTG to emulate inertia and support primary frequency control. The research work [11] introduces time––varying–gain inertia and droop loops to the conventional wind turbine control. The gains are determined according to desired frequency–response time. In VSWTGs, the inertia power is obtained from the kinetic energy in the rotating blades; and the synthetic inertia is limited by the converter power rating, speed, recovery period, etc. [4]. The energy storage systems (ESSs) with efficacious control can act as SGs, hence, injecting (absorbing) power to (from) the grid in response to frequency oscillations. Ref. [12] suggests applying a hybrid ESS (battery and UC) to utility–scale PV units to provide primary frequency control (PFC) and dynamic grid support (DGS). Accordingly, a new voltage––frequency control is proposed, which coordinates the unit MPPT control, the hybrid ESS converter control, and the PV inverter control, resulting in enhanced power grid transient stability. Moreover, a detailed vehicle–to–grid (V2G) model with a fast–responding hybrid ESS is presented in [13] aimed at simultaneously providing the PFC and the DGS. Therein, the V2G converter is governed by a frequency management system without disturbing the scheduled charging–discharging processes. In [14] a virtual inertia emulator–based model predictive control (MPC) is designed for an ESS–fed converter, aiming to find the optimal control operation of the system by predicting its future behaviors. A fuzzy–based hybrid ESS (battery and UC) controller is proposed in [15] for wind power plants. It also introduces a differential evolution–based optimal sizing method for the ESS to obtain the minimum required capacity. Ref. [16] presents ac–coupling of a conventional PV generator and a UC–fed converter. The employed storage includes fast and slow instantaneous power controls. The former controller responds to the intermittent power aimed at smoothing the PV output power. And, the latter controller provides the inertia support to resist grid frequency deviations. The provision of short–term frequency support by the DVI method is discussed in [17] and [18]. Accordingly, the capacitors adhered to the dc–link of grid–connected converters act as the energy buffer for frequency stability enhancement. The DVI is a promising approach in small–scale modern grids dominated by converter–tied generators, and can be implemented without increasing system cost and complexity [17].

1.3. Contribution and paper organization

The major contribution of this work to the research field is summarized as:

- A new DVI–based frequency regulator is first proposed for double––stage PV generators. Unlike the conventional DVI technique [17], the suggested synthetic inertia emulator reverts the dc–link voltage to its nominal value after frequency disturbances occurred in the host grid. Accordingly, better dynamic (slight oscillations) and steady–state performance in the output power and the dc–link voltage is realized.
- Then, the small–signal state–space realization of the PV generator, comprising dynamics of dc/dc and dc/ac converters, interfaced ac filter, synchronization unit, and corresponding controllers, is derived to study the impact of system parameter variations on the generator stability.

The remainder of this work proceeds as follows: Section 2 presents a general configuration of the double–stage PV energy system. The control law and system modeling is provided in Section 3. Section 4 elaborates on the sensitivity of system parameters on the generator stability using small–signal eigenvalue analyses. Simulation results of the proposed control scheme are compared in Section 5 with the conventional DVI method suggested in Ref. [17]. Finally, Section 6 draws the paper conclusion.

2. PV energy system configuration

Throughout this study, complex–valued space vectors - denoted by boldface letters - in synchronous coordinates are used; e.g., the grid voltage vector is $\boldsymbol{u_g} = u_{gd} + ju_{gq}$. The external control set points and internally computed references are marked with "$\star$" in superscripts. The controller operates in PoI voltage–oriented synchronous coordinate, in which $\boldsymbol{u_p} = u_{pd} + j0$. The quantities u_{pv} and i_{pv} are measured aimed at MPPT. The variables $\boldsymbol{i_w}$, $\boldsymbol{u_p}$, and u_{dc} are also sensed for the inverter control.

Figure 1 shows a double–stage PV generator, where the quantities in

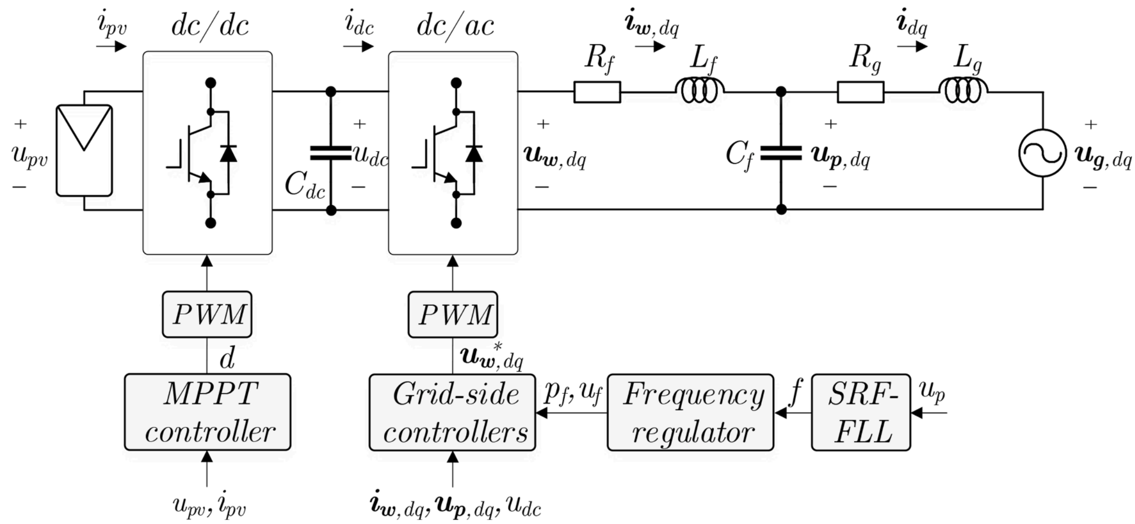

Fig. 1. Block diagram of PV energy system in the SRF.

three–phase side are expressed in the SRF. It comprises a PV array, dc/dc converter, and dc/ac inverter. The dc/dc converter with MPPT keeps the array voltage at a maximum operating point. The inverter converts the dc power to ac power p_w and transmits to the grid through interfaced LC filter. The filter mitigates high–order current harmonics introduced by the switching process. On the dc–side, C_{dc} is the capacitance acting as energy buffer for the grid frequency stability enhancement following supply–demand mismatches, akin to the conventional DVI method [17]. The mechanism of synthetic inertia provision is as follow: any frequency oscillations ($\Delta f = f_0 - f$) is properly linked to the inverter power set point $p_w^\star$. The relevant control architecture is later delineated in Fig. 3. The inertia power is supplied by the capacitor if p_{pv} is constant.

3. Control method and system model

This section details the nonlinear state–space realization for each system element and control block of Fig. 1. Thereafter, the equations are linearized about equilibrium points - signified by "0" in subscripts - for small–signal stability studies.

3.1. Grid model

The ac–side dynamics encompass the LC filter and the host power system. The grid is modeled as Thevenin equivalent with grid strength defined by short–circuit ratio (SCR). If the pulse width modulation (PWM) is fast and accurate, we can consider that the converter voltage command is perfectly transformed to the ac–side, i.e., $\boldsymbol{u}_w = \boldsymbol{u}_w^\star$ [19]. This only disregards the energy loss across the inverter switches. Hence, the underlying dynamics of electric system in the SRF are described by:

$$\dot{\boldsymbol{i}}_w = \frac{1}{L_f}\boldsymbol{u}_w - \frac{1}{L_f}\boldsymbol{u}_p - \left(\frac{R_f}{L_f} + j\omega\right)\boldsymbol{i}_w \tag{1}$$

$$\dot{\boldsymbol{u}}_p = \frac{1}{C_f}\boldsymbol{i}_w - \frac{1}{C_f}\boldsymbol{i} - j\omega\boldsymbol{u}_p \tag{2}$$

$$\dot{\boldsymbol{i}} = \frac{1}{L_g}\boldsymbol{u}_p - \frac{1}{L_g}\boldsymbol{u}_g - \left(\frac{R_g}{L_g} + j\omega\right)\boldsymbol{i}. \tag{3}$$

3.2. Synchronization unit

To synchronize the interfaced inverter with the host grid, the SRF–FLL of Ref. [20] is used here as it enjoys fast and accurate response, and improved filtering performance. The full structure of the SRF–FLL is brought in Fig. 2, which utilizes angular frequency error and phase error information simultaneously. The operating principle is briefly explained as follow. First, the estimation of PoI voltage (i.e. $\widehat{\boldsymbol{u}_p}$) is obtained using a complex low–pass filter as:

$$\dot{\widehat{\boldsymbol{u}_p}} = k_{fll}\left(\boldsymbol{u}_p - \widehat{\boldsymbol{u}_p}\right). \tag{4}$$

To obtain the angular frequency error (ω_e), the imaginary part of the signal $\boldsymbol{u}_p\widehat{\boldsymbol{u}_p}^\star$ is passed through an integrator, in which "$\star$" represents complex conjugate. Then:

$$\omega_e = \underbrace{\frac{k_{fll}d_{fll}}{u_{pd0}^2}\int \underbrace{Im\left(\boldsymbol{u}_p\widehat{\boldsymbol{u}_p}^\star\right)}_{u_{pq}\widehat{u_{pd}} - u_{pd}\widehat{u_{pq}}} dt}_{\phi_\delta}. \tag{5}$$

Different from conventional FLL, the SRF–FLL of Fig. 2 can also provide the phase error information using u_{pq}. Ref. [20] suggests adding the term $u_{pq} - \widehat{u_{pq}}$ associated with the phase error to (5), by which the damping factor of the SRF–FLL is improved. Thus, the synchronization angle is upgraded as:

$$\dot{\delta} = \omega = \omega_0 + \omega_e + \frac{d_{fll}}{u_{pd0}}\left(u_{pq} - \widehat{u_{pq}}\right). \tag{6}$$

3.3. AC current controller (ACC)

The ACC regulates $\boldsymbol{i}_w$ to the current reference space vector $\boldsymbol{i}_w^\star$ by two separate proportional – integral (PI) controllers (cf. Fig. 3). The PoI voltage feedforward, cancellation of the dq cross–coupling, and active resistance term r are considered in the ACC for better dynamics performance and overshoot–rejection capability [21,22]. Thus, the voltage reference $\boldsymbol{u}_w^\star$ to the PWM is given by:

$$\boldsymbol{u}_w^\star = \boldsymbol{u}_p + j\omega L_f\boldsymbol{i}_w - r\boldsymbol{i}_w + k_{pi}\left(\boldsymbol{i}_w^\star - \boldsymbol{i}_w\right) + k_{ii}\underbrace{\int\left(\boldsymbol{i}_w^\star - \boldsymbol{i}_w\right)dt}_{\phi_{i_{w,dq}}}. \tag{7}$$

The reference current $i_{wd}^\star = 2p_w^\star/3u_{pd0}$ is determined by two terms; 1) the dc voltage controller output or p_u, and 2) the frequency regulator output or p_f which are describe in following subsections. And, reactive power requirement defines $i_{wq}^\star = -2q_w^\star/3u_{pd0}$. Using the algorithm given in [22], the controller parameters k_{pi}, k_{ii} and r are set to $\alpha_i L_f$, $\alpha_i^2 L_f$ and $\alpha_i L_f$, respectively; in which α_i is the ACC bandwidth.

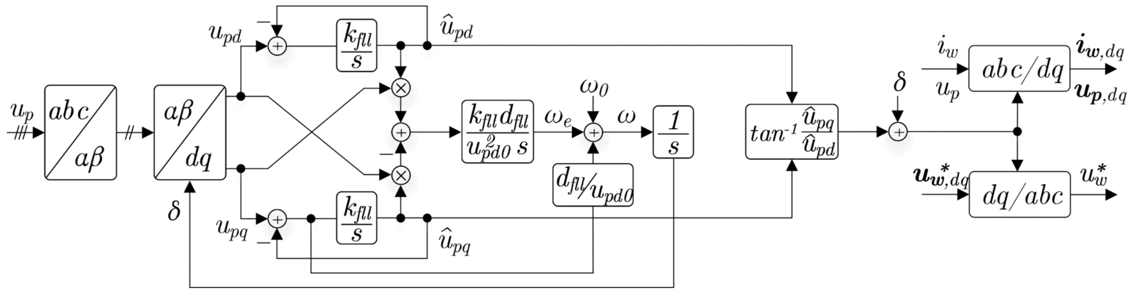

Fig. 2. Block diagram of the SRF–FLL.

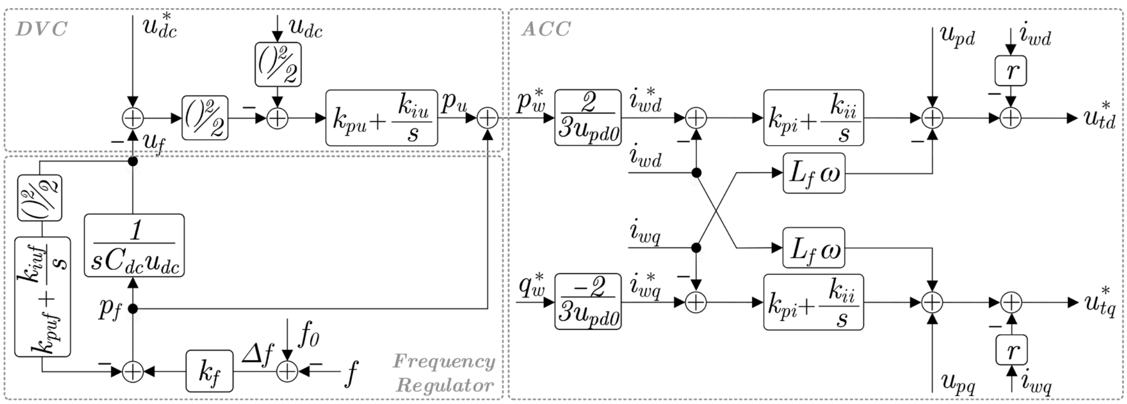

Fig. 3. Grid–following inverter control architecture.

3.4. DC voltage controller (DVC)

The DVC maintains the dc–bus voltage at $u_{dc}^{\star}$. It operates on the error $[u_{dc}^2 - (u_{dc}^{\star} - u_f)^2]/2$ by a PI–controller. The voltage signal u_f is defined later with frequency regulator. The PI parameters correspond to the DVC are selected based on the method in [23] as $k_{pu} = \alpha_u C_{dc}$ with a small k_{iu}. And, α_u is the DVC bandwidth so as it holds $\alpha_u \leq 0.1\alpha_i$; because, as a rule of thumb, the DVC must be slower than the ACC. Then, the DVC output or p_u is described by:

$$p_u = k_{pu}\frac{\left[u_{dc}^2 - (u_{dc}^{\star} - u_f)^2\right]}{2} + \underbrace{k_{iu}\int \frac{\left[u_{dc}^2 - (u_{dc}^{\star} - u_f)^2\right]}{2}dt}_{\phi_u}. \tag{8}$$

3.5. Frequency regulator

Analogous with the DVI method, this loop applies C_{dc} to supply or absorb the inertia power (p_f) when frequency disturbances occur. Then, it improves the grid frequency stability. Here, we implement the DVI idea with a different mechanism from Fang et al. [17]. Unlike [17], however, the dc–bus voltage can reach its nominal after the frequency disturbance.

To this end, Δf is linked to p_f with proportional gain of k_f. But, p_f starts to decay because of the decrease in u_{dc} and the DVC. The decline in dc voltage due to inertia power is obtained as:

$$u_f = \int \frac{p_f}{C_{dc}u_{dc}}dt. \tag{9}$$

This value is added to the DVC (cf. Fig. 3); thus, the variation of u_{dc} caused by the frequency control is excluded from the DVC. Accordingly, p_f is not affected by the DVC and attains the value of $k_f\Delta f$ during frequency disturbance. As per (9), the dc voltage drifts with the time from $u_{dc}^{\star}$. To hold the dc voltage at its reference, u_f must be converged to zero via a PI–controller. The frequency regulator is then revised as:

$$p_f = k_f\Delta f - k_{puf}\frac{u_f^2}{2} - \underbrace{k_{iuf}\int \frac{u_f^2}{2}dt}_{\phi_{uf}} \tag{10}$$

in which the PI parameters are selected so as desired dc voltage recovery time is achieved.

It is noteworthy that the capability of the frequency regulator in enhancing the grid frequency is restricted by the dc–link capacitance size. Hence, following assumptions are considered to calculate the capacitance as a rule of thumb. Consider an extreme case in which the frequency declines by an step–down change with amplitude of Δf during time interval T, and (10) lacks the second and third terms. Thus, the provided energy by the capacitor is equivalent to the orange + gray area shown in Fig. 4; (It is noteworthy that if $p_f = k_f\Delta f$, the dc–link voltage also remains at $u_{dc}^{\star} - u_f$). In reality, however, the injected energy only covers the gray area as all the terms in (10) are considered in the proposed frequency regulator. As per assumptions above, the capacitance is straightforwardly calculated by:

$$\Delta E_f = \frac{1}{2}C_{dc}\Delta u_{dc}^2 = \frac{1}{2}C_{dc}u_{f,\max}^2 \tag{11}$$

$$C_{dc} = \frac{2p_fT}{u_{f,\max}^2} = \frac{2k_f\Delta fT}{u_{f,\max}^2} \tag{12}$$

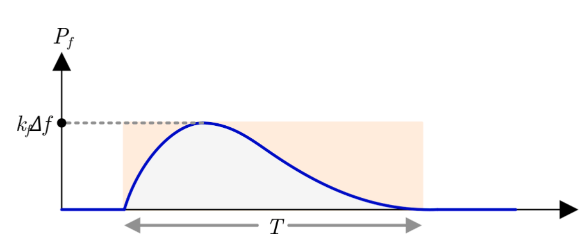

Fig. 4. Injected inertia power for an step–down change in the grid frequency.

where, $u_{f,\max}$ is the maximum permissible dc–link voltage oscillations.

3.6. DC/DC converter and controller

As shown in Fig. 1, the dc–side converter is supplied by the PV array with the model of:

$$u_{pv} = \frac{N_s nkT}{q} \ln\left(\frac{N_p I_{SC} - i_{pv}}{N_p I_0} + 1\right) \tag{13}$$

where the associated quantities are as follows: T, n, I_{SC}, and I_0 are the junction temperature, ideality factor, short–circuit current, and saturation current of the PV cell, respectively. Moreover, k and q are Boltzmann and charge of the electron constants, and N_s and N_p represents number of series and parallel PV panels, respectively. Readers are referred to [24] for small–signal model of the PV array.

The converter boosts the PV array voltage to a suitable level for the inverter dc bus. It is noteworthy that the dc–link voltage maintains at $u_{dc}^{\star}$ by the DVC. Applying state–space averaging method, the equations governing the dynamics of dc/dc converter and dc–link are attained as [25,26]:

$$\dot{i}_{pv} = \frac{1}{L_{pv}} u_{pv} - \frac{1-d}{L_{pv}} u_{dc} \tag{14}$$

$$\dot{u}_{dc} = \frac{1-d}{C_{dc}} i_{pv} - \frac{1}{C_{dc}} i_{dc} \tag{15}$$

in which i_{dc} can be represented by the real power balance between ac– and dc– sides of the inverter as:

$$i_{dc} = \frac{\frac{3}{2}\left(u_{pd} i_{wd} + u_{pq} i_{wq}\right)}{u_{dc}}. \tag{16}$$

Also, the dc/dc converter controller operates on the error signal $i_{pv}^{\star} - i_{pv}$ to provide the control signal d, i.e., the converter duty cycle as:

$$d = k_{pd}\left(i_{pv}^{\star} - i_{pv}\right) + k_{id} \underbrace{\int \left(i_{pv}^{\star} - i_{pv}\right) dt}_{\phi_d} \tag{17}$$

where $i_{pv}^{\star} = p_{pv}/u_{pv}$.

4. Linearized system

The PV generator with the specifications listed in Table 1 is used to study the impact of system parameter variations on the generator stability. The analysis is based on eigenvalues; thus, the Eq. (1)–(17) are linearized about equilibrium points – denoted by subindex "0″ – to obtain the form of [27]:

$$\Delta\dot{x} = \mathbf{A}\Delta x + \mathbf{B}\Delta u \tag{18}$$

where Δx and Δu are the variations of states and input vector. The state and input vectors are defined, respectively as:

$$x = \left[\delta\ \phi_\delta\ i_{wd}\ i_{wq}\ u_{pd}\ u_{pq}\ \widehat{u_{pd}}\ \widehat{u_{pq}}\ i_{pv}\ u_{dc}\ \phi_d\ u_f\ \phi_{uf}\ \phi_u\ \phi_{i_{wd}}\ \phi_{i_{wq}}\ i_d\ i_q\right]^T_{1\times 18} \tag{19}$$

$$u = \left[p_{pv}\ q_w^{\star}\right]^T_{1\times 2}. \tag{20}$$

The associated state and input matrices are provided in Appendix. Table 2 summarizes the pole information of the system. Most of the poles represent non–oscillatory modes, while only four pair of poles represent super–synchronous modes, i.e., frequencies above 50 Hz. Mode 6 has the lowest damping and can cause oscillation due to the low damping level. According to Lyapunov stability theory, the system is asymptotically stable in the small–signal sense. Hereafter, we study the sensitivity of parameters C_{dc}, X/R ratio of the grid (i.e., $2\pi f L_g/R_g$ ratio), grid short–circuit ratio (SCR), and FLL controller gains on the generator stability. In each scenario, other parameters are assumed untouched. Also, the ACC and DVC parameters are regulated as per Sections 3.3 & 3.4, respectively.

First, C_{dc} is scaled using the variable β_{Cdc}, which is increased from 1 to 10 with variations of 1. Figure 5(a) depicts the corresponding pole diagram (only dominant modes are displayed for good visibility). As observed, the poles are scarcely sensitive to the change of dc–link capacitance. Hence, C_{dc} can be enlarged aimed at better primary frequency regulation while the generator remains stable. The small–signal stability analysis of the system under study for different X/R ratios of the host grid is depicted in Fig. 5(b). Accordingly, the X/R ratio is decreased from 7 to 5 with changes of 0.2 (the benchmark is 6.28). As per Fig. 5(b), the dominant modes of 1 to 5 are not sensitive to the X/R ratio variations. Nevertheless, decreasing the X/R ratio yields movement of the mode 6 toward the right–hand side of s–plane, making the system completely unstable for X/R<6. The system stability in terms of different SCRs is shown in Fig. 5(c). Grid strength with SCR<3 yields instability as mode 11 moves toward the right–hand side of s–plane. To overcome this problem, the FLL bandwidth must be reduced (by decreasing k_{fll} and d_{fll}) which subsequently results in a slower transient response [20]. Figure 5 (d) illustrates the eigenvalue loci of the system with SCR = 1 ($R_g = 1\ \Omega$, $L_g =$ 20 mH) when k_{fll} and d_{fll} are multiplied by $0.1 \le \beta_{fll} \le 1$ with variations of 0.1. Reducing $k_{fll} = d_{fll}$ from 41π to 4.1π effectively relocates the unstable mode 11 to the left–half s–plane. However, the response to frequency disturbance, i.e., inertia power injection or absorption, occurs slower as the FLL bandwidth decreases.

5. Results and discussion

5.1. Objective

As stated earlier, the conventional DVI–based synthetic inertia

Table 1
Parameters of the PV generator and the grid.

Parameter	Value	Parameter	Value
R_f, R_g	0.1Ω, 0.1Ω	k_f	3900
L_f, L_g	2.94mH, 2mH	α_i	2π.400rad/s
C_f, C_{dc}	10μF, 10mF	α_u	2π.40rad/s
ω_0	2π.50rad/s	k_{pd}, k_{id}	0.3,20
$u_p^{\star}, u_{dc}^{\star}$	$\sqrt{2/3}$.400V, 750V	k_{fll}, d_{fll}	41π,41π
p_{pv}, $q_w^{\star}$	20kW, 0kVAr	k_{puf}, k_{iuf}	1.5,0.001

Table 2
Pole characteristics.

Mode	Oscil. freq. (Hz)	Damp. ratio (%)
1 : 0	0	100
2 : 0	0	100
3 :≈ 0	0	100
4 : − 0.01	0	100
5 : − 1.2	0	100
6 : − 22.4 ± j7767.2	1236.2	0.29
7 : − 66.7	0	100
8 : − 128.8	0	100
9 : − 128.8	0	100
10 : − 259.5	0	100
11 : − 1559.9 ± j1845.8	293.8	64.6
12 : − 1608.1 ± j937.5	149.2	86.4
13 : − 1854.1 ± j9907.2	1576.8	18.4
14 : − 224072.1	0	100

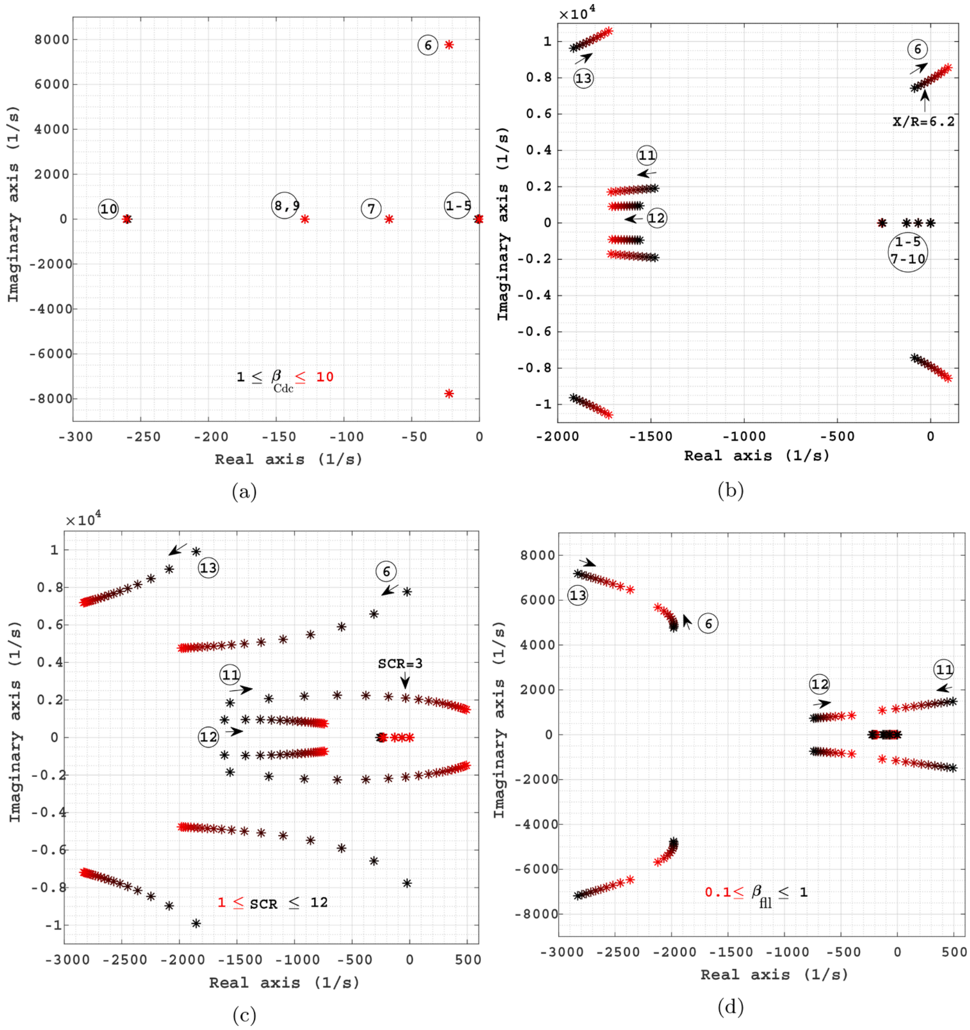

Fig. 5. Impact of parameters a) C_{dc}, b) grid X/R ratio, c) grid SCR, and d) FLL controller gains on the system pole diagram.

emulator of Ref. [17] is modified as Section 3.5 to revert the converter dc–link voltage to its reference after frequency disturbances occurred in the host grid. Accordingly, time–domain simulations are carried out in MATLAB/Simulink to validate the efficacy of the proposed control method. The PV generator augmented with the proposed approach operates under following condition: the operating voltage and power rating are 400 V(rms) and 20 kVA, respectively. The maximum permissible dc–link voltage oscillations is assumed ±50 V. The rest of system parameters are brought in Table 1. Step–changes of ±0.5 Hz in the grid frequency are considered as the input disturbances, and in which scenario the proposed method is compared to Ref. [17]. For a fair comparison, in the two methods 1) the SRF–FLL of Section 3.2 is used for synchronization, and 2) the ACC parameters are set by the technique of Section 3.3 (the DVC parameters are regulated differently as the synthetic inertia emulators are different).

5.2. Results

We first study −0.5 Hz step–change in the frequency scenario. Figure 6 depicts the SRF–FLL response, by which perfect grid synchronization is obtained in 0.04 s. It is noteworthy that large FLL bandwidth induces instability to the controller as discussed in Section 4. In contrast, slow grid synchronization reduces the effectiveness of the synthetic inertia emulator. The PV generator augmented with the frequency regulator of this paper and [17] is simulated separately; and the corresponding results are illustrated in Fig. 7. As observed from this figure, each PV generator injects 20 kW active power in the steady state condition, but p_w increases to about 22 kW following the defined disturbance by means of the frequency regulators (i.e., mechanism of synthetic inertia provision). Compared to [17], the proposed method provides a faster response to curb the disturbance. The inertia power of ≈2 kW is

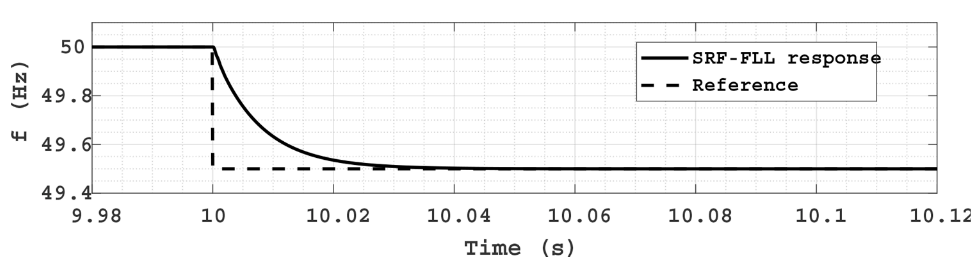

Fig. 6. Response of synchronization unit in the first case study.

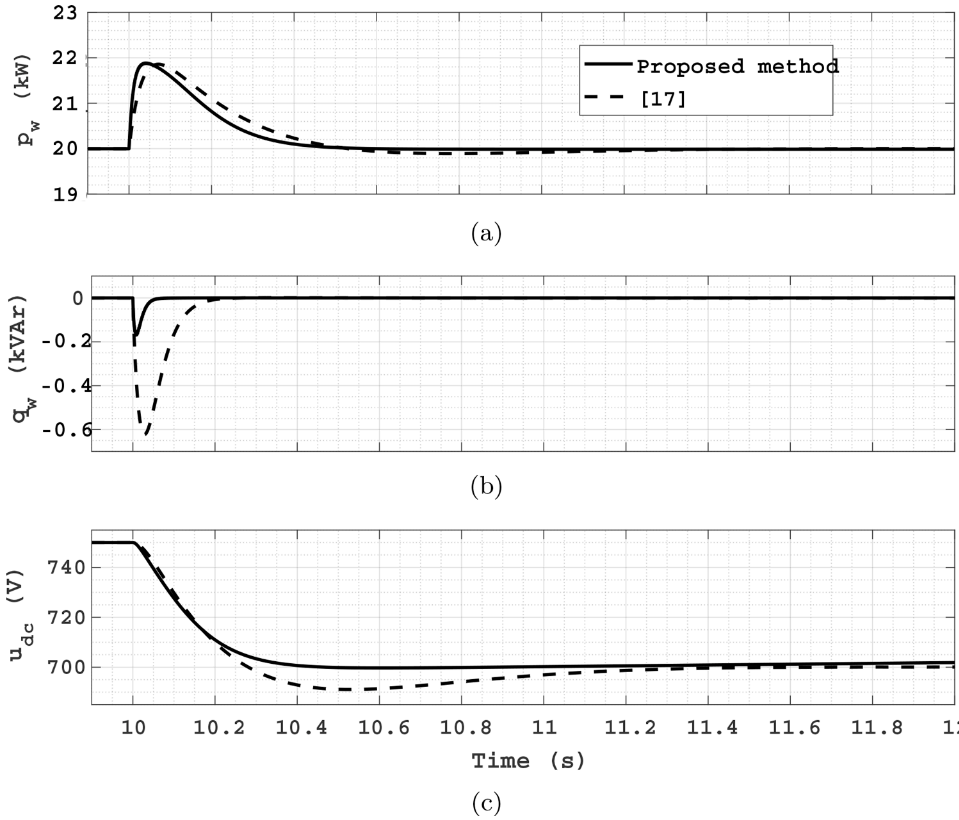

Fig. 7. Inverter outputs (remark: step–down change in the frequency occurs at $t = 10$ s).

supplied by discharging the dc–link capacitance, which is analogous with the released kinetic energy of SGs to regain the power balance during the transient. Figure 7(b) shows the exchanged reactive power between the PV generator and the host grid. It can be seen that q_w peaks at –0.17 and –0.62 kVAr by the proposed approach and [14], respectively; and the reactive power reaches four times faster to its nominal with the proposed method. Also, the dc–bus voltage oscillations in case of applying proposed synthetic inertia emulator and the method of [17] are demonstrated in Fig. 7(c). With [17], the voltage first exceeds the acceptable range by −12 V and then remains at 700 V after 1.2 s. In other words, it does not revert to the reference. Hence, undesirable overmodulation in the controller may arise especially after cascading frequency events [28]. This problem is solved by the proposed outer–loop controller of Fig. 3; i.e., 1) the dc–link voltage stays within the permissible range without any oscillation [cf. Fig. 7(c)], and 2) it converges to the reference of 750 V after providing synthetic inertia support to the host grid as shown in Fig. 8. From Figs. 7 & 8, we conclude that better dynamic (i.e., slight oscillation) and steady–state performance in the output power and the dc–link voltage is achieved with the proposed control scheme.

Similar results are attained if the grid is subject to a + 0.5 Hz step–change in the frequency; i.e., f becomes larger than its nominal value. This scenario accelerates the rotors and increases the mechanical stress of SGs operating in the grid. This issue can be addressed by adopting proper synthetic inertia emulator. Fig. 9 presents the SRF–FLL response in tracking the frequency. Again, it synchronizes the PV generator with the new grid frequency within 0.04 s. The generator active power and its associated inertia power functioned by the proposed frequency regulator and the method of [17] are depicted in Fig. 10 (a). As illustrated in this figure, the output power is 20 kW in the steady–state operation. However, it curtails to about 18 kW after the disturbance, i.e., the inverter charges the dc–link capacitor by absorbing ≈2 kW power from the grid to attenuate the frequency rate of change. This mechanism is analogous with the absorbed kinetic energy of real SGs to slow down the grid frequency dynamics (RoCoF) during transients. Figure 10(b) depicts the corresponding reactive power. It is clear that q_w has a slight overshoot and reaches its reference faster when the proposed technique is applied. The dc–side voltage is also brought in Fig. 10(c). Again, unlike [17], the proposed method holds the dc–link voltage within the acceptable range and reverts it to the nominal value after the input disturbance [cf. Figs. 10(c) & 11]. Thus, the dc–link voltage restoration problem in the conventional DVI approach is solved

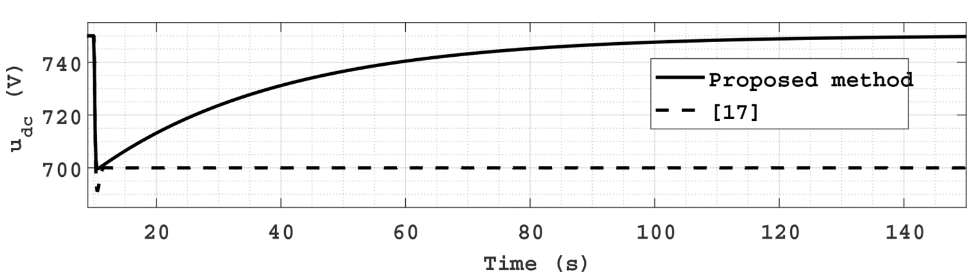

Fig. 8. Inverter dc–link voltage in the first case study.

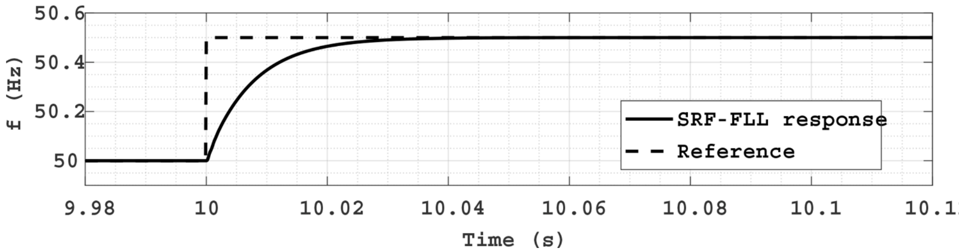

Fig. 9. Response of synchronization unit in the second case study.

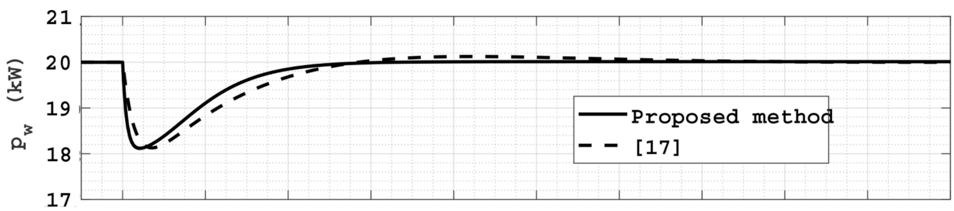

(a)

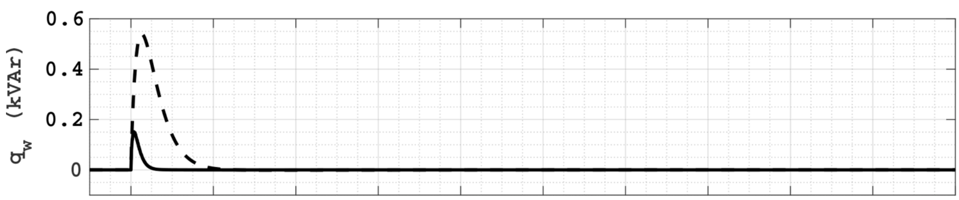

(b)

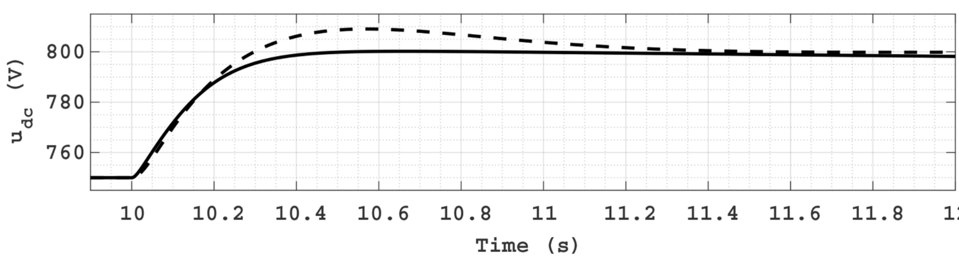

(c)

Fig. 10. Inverter outputs (remark: step–up change in the frequency occurs at $t = 10$ s).

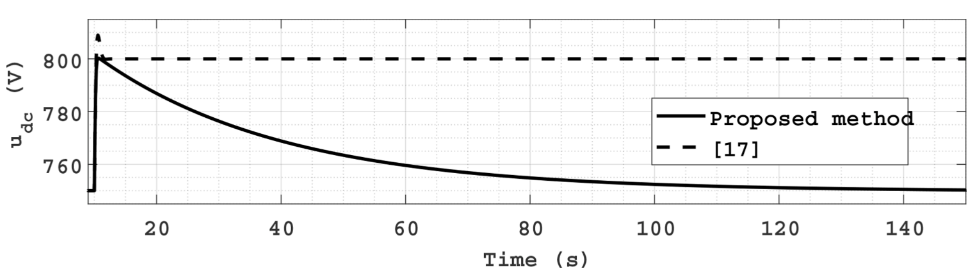

Fig. 11. Inverter dc–link voltage in the second case study.

by applying the proposed method.

Next, the frequency response of the grid with and without synthetic inertia provision is studied to validate the effectiveness of the proposed frequency regulator in curtailing the RoCoF level. To this end, the grid is modeled by an SG, operating in the following condition: the line–to–line voltage and the nominal power are 400 V(rms) and 20 kVA, and the inertia and the damping factor are 5 s and 1, respectively. Furthermore, a governor with droop characteristic of 5% and 0.2 s time constant, and IEEE type AC5A excitation system regulate the SG mechanical input and the field voltage, respectively. The SG in cooperation with the PV generator understudy supplies power to a local load of 40 kW. Again, two scenarios are considered, i.e., $\pm 10\%$ sudden change in the load at $t = 10$ s. In each case study, the grid frequency is then measured with and without considering provision of the synthetic inertia.

Figure 12 (a) depicts the grid frequency response of step–up change in the demand scenario. When the PV generator is augmented with the

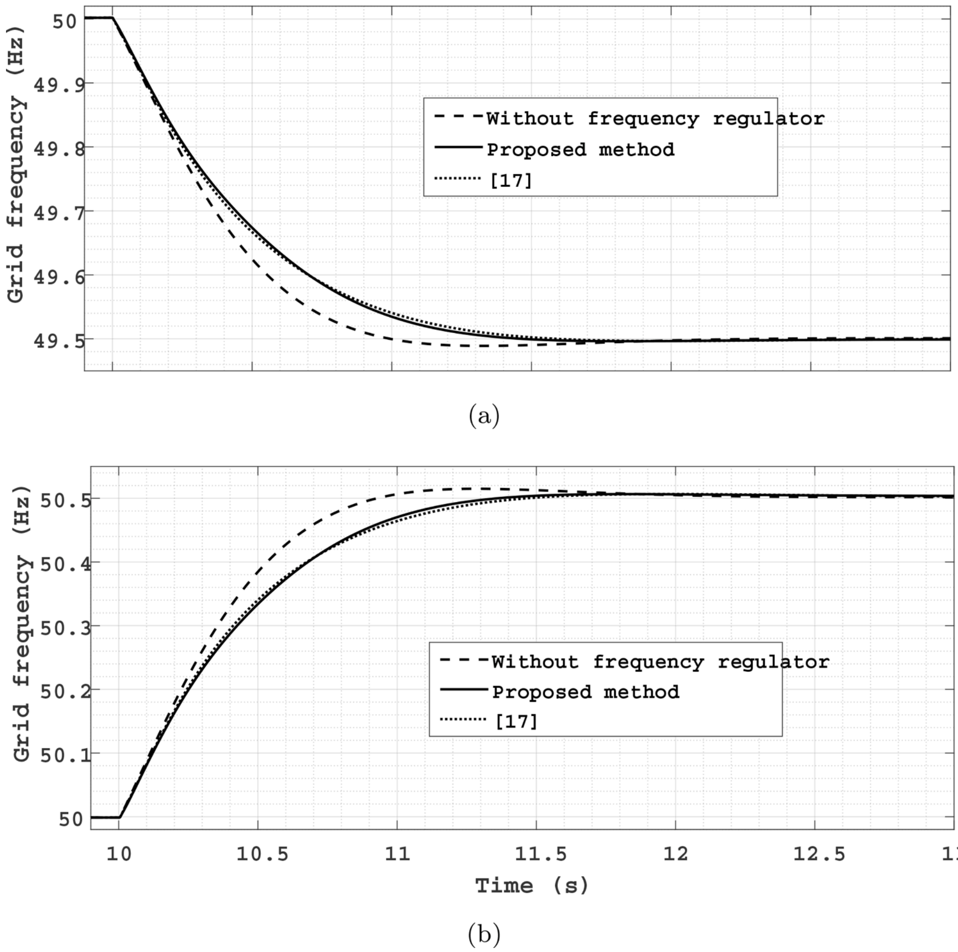

Fig. 12. Grid frequency response under 10% a) step–up, b) step–down change in the load at $t = 10$ s.

proposed frequency regulator, the grid experiences lower frequency nadir. Also, the RoCoF is improved from 0.82 Hz/s to 0.7 Hz/s (i.e., 14.6% enhancement in the RoCoF level collated with the case in which the synthetic inertia emulator staying nullified). The same results are obtained if step–down change in the demand occurs. As observed from Fig. 12(b), the maximum frequency deviation and the RoCoF level are improved when the synthetic inertia emulator is applied. It is noteworthy that the proposed frequency regulator and the conventional DVI technique yield almost the same frequency stability enhancement (i.e., 14.6% improvement in the RoCoF). However, the method of this paper provides better dynamic and steady–state performance in the output power and the dc–link voltage as shown in Figs. 7 & 8.

6. Conclusion

This work presented a double–stage PV generator equipped with a modified DVI–based grid frequency regulator. Akin to the conventional DVI method [17], the proposed synthetic inertia emulator utilized the inverter dc–side capacitor as the energy buffer. Hence, it improved the grid frequency stability by discharging or charging the dc–link capacitor. Compared to [17], 1) the suggested method enjoyed better dynamic performance (i.e., slight oscillations in the output power and the dc–link voltage), and 2) it reverted the dc–bus voltage to its nominal after the frequency disturbance occurred in the host grid. Small–signal state–-space analyses were conducted to study the impact of different dc–side capacitance, X/R ratio of the grid, grid SCR, and FLL controller gains on the generator stability. The stability evaluations shown that the system under study is subjected to instability for X/R<6 and SCR<3. Moreover, simulations depicted that a 14.6% improvement of frequency rate of change can be obtained by the proposed synthetic inertia emulator compared to the case in which the frequency regulator is nullified.

Credit Author Statement

All persons who meet authorship criteria are listed as authors, and all authors certify that they have participated sufficiently in the work to take public responsibility for the content, including participation in the concept, design, analysis, writing, or revision of the manuscript. Furthermore, each author certifies that this material or similar material has not been and will not be submitted to or published in any other publication before its appearance in the Electric Power Systems Research (EPSR) journal.

CRediT authorship contribution statement

Meysam Saeedian: Conceptualization, Methodology, Software, Formal analysis, Writing – original draft. **Shamsodin Taheri:** Conceptualization, Methodology, Writing – review & editing. **Edris Pouresmaeil:** Conceptualization, Methodology, Supervision, Writing – original draft, Writing – review & editing.

Declaration of Competing Interest

The authors declare that they have no known competing financial interests or personal relationships that could have appeared to influence the work reported in this paper.

Appendix. State and input matrices

$A(i,j)$ denotes the element of row i and column j in the state matrix $\mathbf{A}_{18\times18}$.

$\rightarrow A(1,2)=1;\ A(1,6)=\frac{d_{fll}}{u_{pd0}};\ A(1,8)=\frac{-d_{fll}}{u_{pd0}};$

$\rightarrow A(2,5)=\frac{-k_{fll}d_{fll}\widehat{u_{pq0}}}{u_{pd0}^2};\ A(2,6)=\frac{k_{fll}d_{fll}\widehat{u_{pd0}}}{u_{pd0}^2};\ A(2,7)=\frac{k_{fll}d_{fll}u_{pq0}}{u_{pd0}^2};\ A(2,8)=\frac{-k_{fll}d_{fll}}{u_{pd0}};$

$\rightarrow A(3,2)=\frac{-k_{pi}k_f}{3\pi L_f u_{pd0}};\quad A(3,3)=-\frac{k_{pi}+r+R_f}{L_f};\quad A(3,5)=\frac{-1}{L_f};\quad A(3,6)=\frac{-k_{pi}d_{fll}k_f}{3\pi L_f u_{pd0}^2};\quad A(3,8)=\frac{k_{pi}d_{fll}k_f}{3\pi L_f u_{pd0}^2};\quad A(3,10)=\frac{2k_{pi}k_{pu}u_{dc0}+2k_{pi}k_{pu}u_{f0}}{3L_f u_{pd0}};\quad A(3,12)=\frac{2k_{pi}k_{pu}u_{f0}-2k_{pi}k_{puf}u_{f0}+2k_{pi}k_{pu}u_{dc0}}{3L_f u_{pd0}};\ A(3,13)=\frac{-2k_{pi}}{3L_f u_{pd0}};\ A(3,14)=\frac{2k_{pi}}{3L_f u_{pd0}};\ A(3,15)=\frac{1}{L_f};$

$\rightarrow A(4,4)=-\frac{k_{pi}+r+R_f}{L_f};\ A(4,6)=\frac{-1}{L_f};\ A(4,16)=\frac{1}{L_f};$

$\rightarrow A(5,2)=u_{pq0};\ A(5,3)=\frac{1}{C_f};\ A(5,6)=\omega_0+\frac{u_{pq0}d_{fll}}{u_{pd0}};\ A(5,8)=\frac{-u_{pq0}d_{fll}}{u_{pd0}};\ A(5,17)=\frac{-1}{C_f};$

$\rightarrow A(6,2)=-u_{pd0};\ A(6,4)=\frac{1}{C_f};\ A(6,5)=-\omega_0;\ A(6,6)=-d_{fll};\ A(6,8)=d_{fll};\ A(6,18)=\frac{-1}{C_f};$

$\rightarrow A(7,5)=k_{fll};\ A(7,7)=-k_{fll};$

$\rightarrow A(8,6)=k_{fll};\ A(8,8)=-k_{fll};$

$\rightarrow A(9,9)=\frac{g-k_{pd}u_{dc0}}{L_{pv}}-\frac{gk_{pd}p_{pv0}u_{dc0}}{L_{pv}u_{pv0}^2};\ A(9,10)=\frac{d_0-1}{L_{pv}};\ A(9,11)=\frac{u_{dc0}}{L_{pv}};$

$\rightarrow A(10,1)=\frac{-1.5i_{wd0}u_{pq0}+1.5i_{wq0}u_{pd0}}{C_{dc}u_{dc0}};\quad A(10,3)=\frac{-1.5u_{pd0}}{C_{dc}u_{dc0}};\quad A(10,4)=\frac{-1.5u_{pq0}}{C_{dc}u_{dc0}};\quad A(10,5)=\frac{-1.5i_{wd0}}{C_{dc}u_{dc0}};\quad A(10,6)=\frac{-1.5i_{wq0}}{C_{dc}u_{dc0}};\quad A(10,9)=\frac{1-d_0+k_{pd}i_{pv0}}{C_{dc}}+\frac{gk_{pd}i_{pv0}p_{pv0}}{C_{dc}u_{pv0}^2};\ A(10,10)=\frac{i_{dc0}}{C_{dc}u_{dc0}};\ A(10,11)=\frac{-i_{pv0}}{C_{dc}};$

$\rightarrow A(11,9)=\frac{-gk_{id}p_{pv0}}{u_{pv0}^2}-k_{id};$

$\rightarrow A(12,2)=\frac{-k_f}{2\pi C_{dc}u_{dc0}};\ A(12,6)=\frac{-k_f d_{fll}}{2\pi C_{dc}u_{dc0}u_{pd0}};\ A(12,8)=\frac{k_f d_{fll}}{2\pi C_{dc}u_{dc0}u_{pd0}};\ A(12,12)=\frac{-k_{puf}u_{f0}}{C_{dc}u_{dc0}};\ A(12,13)=\frac{-1}{C_{dc}u_{dc0}};$

$\rightarrow A(13,12)=k_{iuf}u_{f0};$

$\rightarrow A(14,10)=k_{iu}u_{dc0}+k_{iu}u_{f0};\ A(14,12)=k_{iu}u_{f0}+k_{iu}u_{dc0};$

$\rightarrow A(15,2)=\frac{-k_f k_{ii}}{3\pi u_{pd0}};\quad A(15,3)=-k_{ii};\quad A(15,6)=\frac{-k_f k_{ii}d_{fll}}{3\pi u_{pd0}^2};\quad A(15,8)=\frac{k_f k_{ii}d_{fll}}{3\pi u_{pd0}^2};\quad A(15,10)=\frac{2k_{ii}k_{pu}u_{dc0}+2k_{ii}k_{pu}u_{f0}}{3u_{pd0}};\quad A(15,12)=\frac{2k_{ii}k_{pu}u_{f0}-2k_{ii}k_{puf}u_{f0}+2k_{ii}k_{pu}u_{dc0}}{3u_{pd0}};\ A(15,13)=\frac{-2k_{ii}}{3u_{pd0}};\ A(15,14)=\frac{2k_{ii}}{3u_{pd0}};$

$\rightarrow A(16,4)=-k_{ii};$

$\rightarrow A(17,2)=i_{q0};\ A(17,5)=\frac{1}{L_g};\ A(17,6)=\frac{i_{q0}d_{fll}}{u_{pd0}};\ A(17,8)=\frac{-i_{q0}d_{fll}}{u_{pd0}};\ A(17,17)=\frac{-R_g}{L_g};\ A(17,18)=\omega_0;$

$\rightarrow A(18,2)=-i_{d0};\ A(18,6)=\frac{1}{L_g}-\frac{i_{d0}d_{fll}}{u_{pd0}};\ A(18,8)=\frac{i_{d0}d_{fll}}{u_{pd0}};\ A(18,17)=-\omega_0;\ A(18,18)=\frac{-R_g}{L_g};$

Also, $B(i,j)$ denotes the element of row i and column j in the input matrix $\mathbf{B}_{18\times2}$.

$\rightarrow B(4,2)=\frac{-2k_{pi}}{3L_f u_{pd0}};$

$\rightarrow B(9,1)=\frac{k_{pd}u_{dc0}}{L_{pv}u_{pv0}};$

$\rightarrow B(10,1)=\frac{-k_{pd}i_{pv0}}{C_{dc}u_{pv0}};$

$\rightarrow B(11,1)=\frac{k_{id}}{u_{pv0}};$

$\rightarrow B(16,2)=\frac{-2k_{ii}}{3u_{pd0}};$

The rest of elements in $\mathbf{A}$ and $\mathbf{B}$ are zero.

References

[1] A.S. Ahmadyar, S. Riaz, G. Verbič, et al., A framework for assessing renewable integration limits with respect to frequency performance, IEEE Trans. Power Syst. 33 (4) (2018) 4444–4453.

[2] P.G. Bueno, J.C. Hernández, F.J. Ruiz-Rodriguez, Stability assessment for transmission systems with large utility-scale photovoltaic units, IET Renew. Power Gener. 10 (5) (2016) 584–597.

[3] R. Mandal, K. Chatterjee, Virtual inertia emulation and RoCoF control of a microgrid with high renewable power penetration, Electr. Power Syst. Res. 194 (2021) 107093, https://doi.org/10.1016/j.epsr.2021.107093.

[4] H. Bevrani, H. Golpîra, A.R. Messina, et al., Power system frequency control: an updated review of current solutions and new challenges, Electr. Power Syst. Res. 194 (2021) 107114, https://doi.org/10.1016/j.epsr.2021.107114.

[5] A. Moeini, I. Kamwa, Analytical concepts for reactive power based primary frequency control in power systems, IEEE Trans. Power Syst. 31 (6) (2016) 4217–4230.

[6] Q. Zhong, G. Weiss, Synchronverters: inverters that mimic synchronous generators, IEEE Trans. Ind. Electron. 58 (4) (2011) 1259–1267.

[7] S. Dong, Y.C. Chen, A method to directly compute synchronverter parameters for desired dynamic response, IEEE Trans. Energy Convers. 33 (2) (2018) 814–825.

[8] M. Ashabani, F.D. Freijedo, S. Golestan, J.M. Guerrero, Inducverters: PLL-less converters with auto-synchronization and emulated inertia capability, IEEE Trans. Smart Grid 7 (3) (2016) 1660–1674.

[9] D.M. Magnus, C.C. Scharlau, L.L. Pfitscher, et al., A novel approach for robust control design of hidden synthetic inertia for variable speed wind turbines, Electric Power Syst. Res. 196 (2021) 107267, https://doi.org/10.1016/j.epsr.2021.107267.

[10] X. Yingcheng, T. Nengling, Review of contribution to frequency control through variable speed wind turbine, Renew. Energy 36 (2011) 1671–1677.

[11] Y. Wu, W. Yang, Y. Hu, P.Q. Dzung, Frequency regulation at a wind farm using time-varying inertia and droop controls, IEEE Trans. Ind. Appl. 55 (1) (2019) 213–224.

[12] J.C. Hernández, P.G. Bueno, F. Sanchez-Sutil, Enhanced utility-scale photovoltaic units with frequency support functions and dynamic grid support for transmission systems, IET Renew. Power Gener. 11 (3) (2017) 361–372.

[13] J.C. Hernández, F. Sanchez-Sutil, P.G. Vidal, C. Rus-Casas, Primary frequency control and dynamic grid support for vehicle-to-grid in transmission systems, Int. J. Electr. PowerEnergy Syst. 100 (2018) 152–166.

[14] N. Sockeel, J. Gafford, B. Papari, M. Mazzola, Virtual inertia emulator-based model predictive control for grid frequency regulation considering high penetration of inverter-based energy storage system, IEEE Trans. Sustain. Energy 11 (4) (2020) 2932–2939.

[15] J. Cao, W. Du, H. Wang, M. McCulloch, Optimal sizing and control strategies for hybrid storage system as limited by grid frequency deviations, IEEE Trans. Power Syst. 33 (5) (2018) 5486–5495.

[16] X. Quan, R. Yu, X. Zhao, et al., Photovoltaic synchronous generator: Architecture and control strategy for a grid-forming PV energy system, IEEE Jour. Emerg. Selec. Top. Power Electron. 8 (2) (2020) 936–948.

[17] J. Fang, H. Li, Y. Tang, F. Blaabjerg, Distributed power system virtual inertia implemented by grid-connected power converters, IEEE Trans. Power Electron. 33 (10) (2018) 8488–8499.

[18] M. Saeedian, B. Eskandari, S. Taheri, et al., A control technique based on distributed virtual inertia for high penetration of renewable energies under weak

grid conditions, IEEE Syst. J. (2020), https://doi.org/10.1109/JSYST.2020.2997392.
[19] L. Harnefors, Analysis of subsynchronous torsional interaction with power electronic converters, IEEE Trans. Power Syst. 22 (1) (2007) 305–313.
[20] X. Quan, Q. Hu, A.Q. Huang, et al., A novel synchronous reference frame frequency-locked loop, arXiv preprint arXiv:1908.08669(2019).
[21] F.B. del Blanco, M.W. Degner, R.D. Lorenz, Dynamic analysis of current regulators for AC motors using complex vectors, IEEE Trans. Ind. Appl. 35 (6) (1999) 1424–1432.
[22] L. Harnefors, L. Zhang, M. Bongiorno, Frequency-domain passivity-based current controller design, IET Power Electron. 1 (4) (2008) 455–465.
[23] L. Harnefors, M. Bongiorno, S. Lundberg, Input-admittance calculation and shaping for controlled voltage-source converters, IEEE Trans. Ind. Electron. 54 (6) (2007) 3323–3334.
[24] Z. Moradi-Shahrbabak, A. Tabesh, Effects of front-end converter and DC-link of a utility-scale PV energy system on dynamic stability of a power system, IEEE Trans. Ind. Electron. 65 (1) (2018) 403–411.
[25] D.W. Hart, Power Electronics, McGraw-Hill, New York, NY, USA, 2010.
[26] J. Mahdavi, A. Emaadi, M.D. Bellar, M. Ehsani, Analysis of power electronic converters using the generalized state-space averaging approach, IEEE Trans. Circuits and Systems I: Fundamental Theory and Applications 44 (8) (1997) 767–770.
[27] P. Kundur, Power System Stability and Control, first ed., McGraw-Hill Education, 1994.ISBN-13: 978-0070359581
[28] D.G. Holmes, T.A. Lipo, Pulse Width Modulation for Power Converters: Principles and Practice, John Wiley & Sons, 2003.ISBN: 978-0-471-20814-3, 18